JOURNAL OF SOLID STATE CHEMISTRY 83, 20–30 (1989)

Crystal Structure and Magnetism in $CoSb_2O_6$ and $CoTa_2O_6$

J. N. REIMERS, J. E. GREEDAN, C. V. STAGER, AND R. KREMER*

Institute for Materials Research and The McMaster Nuclear Reactor, McMaster University, Hamilton, Canada L8S 4M1

Received April 19, 1989

$CoSb_2O_6$ was investigated by neutron diffraction and magnetic susceptibility techniques. The structure found was tetragonal, of the trirutile type, with space group $P4_2/mnm$, $a = 4.6495(2)$ Å, $c = 9.2763(6)$ Å. Low-temperature neutron data gave no evidence of structural change down to 20 K. Susceptibility data showed a deviation from Curie–Weiss behavior below 100 K and a maximum at 35 K associated with low-dimensional ordering. A Curie–Weiss law fit of the data above 100 K gave $\mu_{eff} = 4.62(1)\ \mu_B$ and $\theta = -32.4(3)$ K. The ordered magnetic structure as determined by neutron diffraction was indexed on a supercell ($2a$, a, $2c$) and is similar to that found previously for $FeTa_2O_6$. Measured magnetic moments below T_c gave an extrapolated zero-temperature moment of $3.3(2)\ \mu_B$ for Co^{2+} and critical parameters $\beta = 0.12(2)$ and $T_c = 12.64(5)$ K, consistent with the two-dimensional Ising model. The crystal structure of $CoTa_2O_6$ was found to be the same as that for $CoSb_2O_6$ with $a = 4.7358(3)$ Å and $c = 9.1708(7)$ Å and with no structural change down to 10 K. At 4.2 K magnetic reflections were observed that could be indexed with a propagation vector $\mathbf{k}_0 = (\frac{1}{4}, \frac{1}{4}, \frac{1}{2})$. A two-cone axis helical spin structure is proposed which can account for the observed intensities. Some of the differences in magnetic properties of the two compounds can be understood in terms of bond distances within the Co–O layers.

Introduction

Materials with the composition MTa_2O_6, M = V, Fe, Co, Ni, all of which crystallize in the trirutile structure, have been investigated recently in our laboratories. Similarities between the trirutile and the K_2NiF_4 structures led to studies of the magnetic properties of these tantalates which have disclosed considerable evidence for short-range magnetic correlations extending over the temperature range 15–40 K and long-range magnetic order below 6–10 K for $FeTa_2O_6$, $CoTa_2O_6$, and $NiTa_2O_6$ (*1–3*). For $CoTa_2O_6$ the analysis of heat capacity data is consistent with a two-dimensional Ising model for the ordered state, $T_N = 6.6$ K, showing strong intraplane anisotropy, $J_1/J_2 = 60$, and a nearly linear chain model for the short-range ordered regime (*2, 3*). Neither a detailed crystal structure nor a magnetic structure has been reported for $CoTa_2O_6$.

$CoSb_2O_6$ is also reported to crystallize in the trirutile structure (*4*). It is of interest to determine the consequences of the substitution of Sb^{5+} for Ta^{5+} on the magnetic properties. As a first effort to study the effect of this substitution, the crystal structure and magnetic properties (including

* Current address: Max Plank Institute fur Festkoerperforschung, Heisenbergstrasse 1, D-7000, Stuttgart 80, FRG.

0022-4596/89 $3.00

magnetic structure and critical behavior) of $CoSb_2O_6$ were investigated and compared with corresponding results for $CoTa_2O_6$.

Experimental Details

The $CoSb_2O_6$ sample was an orange-brown powder prepared from CoO and Sb_2O_3. A slight excess (5%) of Sb_2O_3 was added to prevent the formation of $Co_7Sb_2O_{12}$ (*5*). The sample was heated in an Al_2O_3 crucible at a rate of 50°C/day from 400 to 1050°C and then left at 1050°C for 3 days. Two regrindings and refirings at 1050°C were necessary to obtain a pure phase.

$CoTa_2O_6$ was prepared by heating, in a platinum crucible, stoichiometric amounts of CoO and Ta_2O_5 in the form of pressed pellets. The reaction was carried out in air at 1050°C for a period of 2 days. Regrinding and refiring were necessary in order to obtain a single-phase sample (*6*).

Powder neutron diffraction data were obtained at the McMaster Nuclear Reactor with 1.3913-Å neutrons. Data sets at 298, 20, and 7 K and 20 temperatures between 7 and 13 K were collected for $CoSb_2O_6$. For $CoTa_2O_6$, data sets at 298, 77, 15, and 4.2 K were collected. The detector was a three-tube position-sensitive detector which has been described previously, (*7, 8*). For the room-temperature experiments the sample was held in a thin-walled vanadium can. For low temperatures the sample was contained in an aluminum can along with helium exchange gas and sealed with an indium gasket.

Structure refinements were carried out by the Rietveld profile refinement method (*9*). The magnetic structures were refined using a profile-fitting program developed locally for handling magnetic super-lattice and incommensurate structures, (*8*). Neutron-scattering lengths were taken from Koester (*10*) and the magnetic form factor for Co^{2+} was taken from Watson and Freeman (*11*). No corrections for absorption, extinction, or preferred orientation were applied.

Magnetic susceptibility data were collected on a Quantum Design SQUID magnetometer using a pressed polycrystalline pellet. The magnetometer was calibrated with high-purity palladium.

Results and Discussion

$CoSb_2O_6$ Structure Data

The expected trirutile structure was verified. The cell constants are smaller than those reported by Kasper (*4*) from X-ray work, but are not significantly different within the limit of three standard deviations. These results are shown in Table I and the profile fit is shown in Fig. 1.

The crystal structure remains unchanged down to 20 K with only small changes in positional parameters, of the order of .01 Å.

Nearest-neighbor bond distances from the 298 K data are shown in Table II and exhibit no anomalous behavior when com-

TABLE I

CRYSTALLOGRAPHIC PARAMETERS FOR $CoSb_2O_6$ AT ROOM TEMPERATURE

Atom	Position	x	y	z	B(Å^2)
Co	2*a*	0	0	0	1.0(3)
Sb	4*e*	0	0	0.3358(9)	0.12(6)
O_1	4*f*	0.3082(9)	0.3082(9)	0	0.4(1)
O_2	8*j*	0.3026(5)	0.3026(5)	0.3264(5)	0.34(6)
R_{wp}[a]			5.5%		
R_p[b]			4.2%		
R_{nuc}[c]			4.2%		
R_{exp}[d]			1.4%		
No. of data points			1045		
Ind. reflections			113		
d-Space range (Å)			0.849–4.65		

Note. Space group $P4_2/mnm$; $Z = 2$; $a = 4.6495(2)$ Å; $c = 9.2763(6)$ Å; vol. = 200.53(3) Å^3.

[a] Weighted profile $R_{wp} = 100 \times \{[\Sigma w(Y_{obs} - Y_{calc})^2]/[\Sigma w(Y_{obs})^2]\}^{1/2}$.

[b] Profile $R_p = 100 \times \Sigma|Y_{obs} - Y_{calc}|/\Sigma Y_{obs}$.

[c] Nuclear $R_{nuc} = 100 \times \Sigma|I_{obs} - I_{cal}|/\Sigma I_{obs}$.

[d] Expected $R_{exp} = 100 \times \{(N - P)/\Sigma w(Y_{obs})^2\}^{1/2}$.

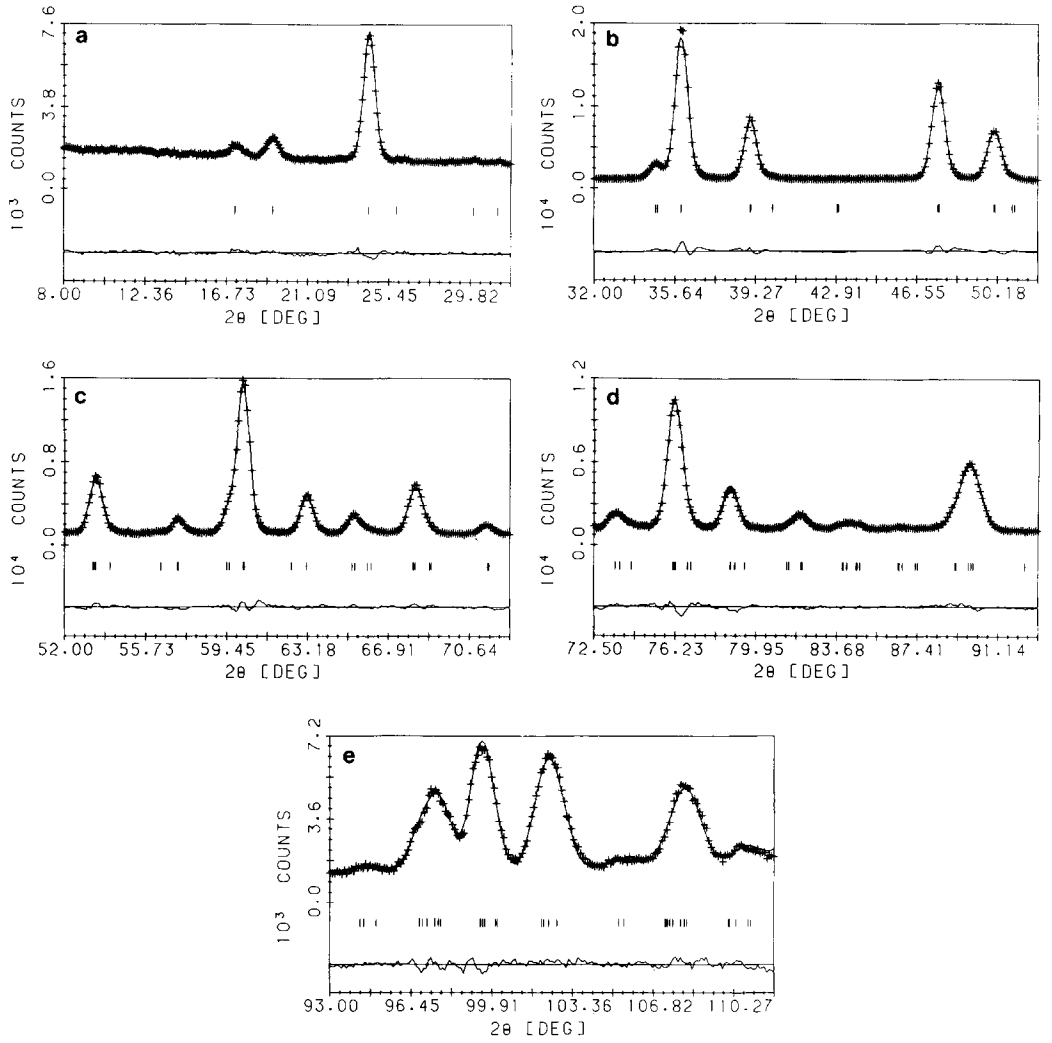

FIG. 1. The observed (+), calculated (−), and difference powder profiles for $CoSb_2O_6$ at 298 K (reflection positions are marked).

pared to value expected from summation of atomic radii (*12*).

$CoTa_2O_6$ Structure

Similar results were obtained for the tantalum compound. Again no notable structural changes were observed down to 10 K and the cell volume also remained the same within error. The structural parameters obtained from the profit fit (Fig. 2) are listed in Table III and Table IV lists the bond distances and angles.

Magnetic Susceptibility ($CoSb_2O_6$)

Susceptibility data (Fig. 3) show a broad maximum at ≈35 K, indicative of short-range order. An inflection point is also present below 20 K, indicating a transition to long-range order. Both of these effects are seen clearly in a plot of $d(\chi T)/dT$ vs T

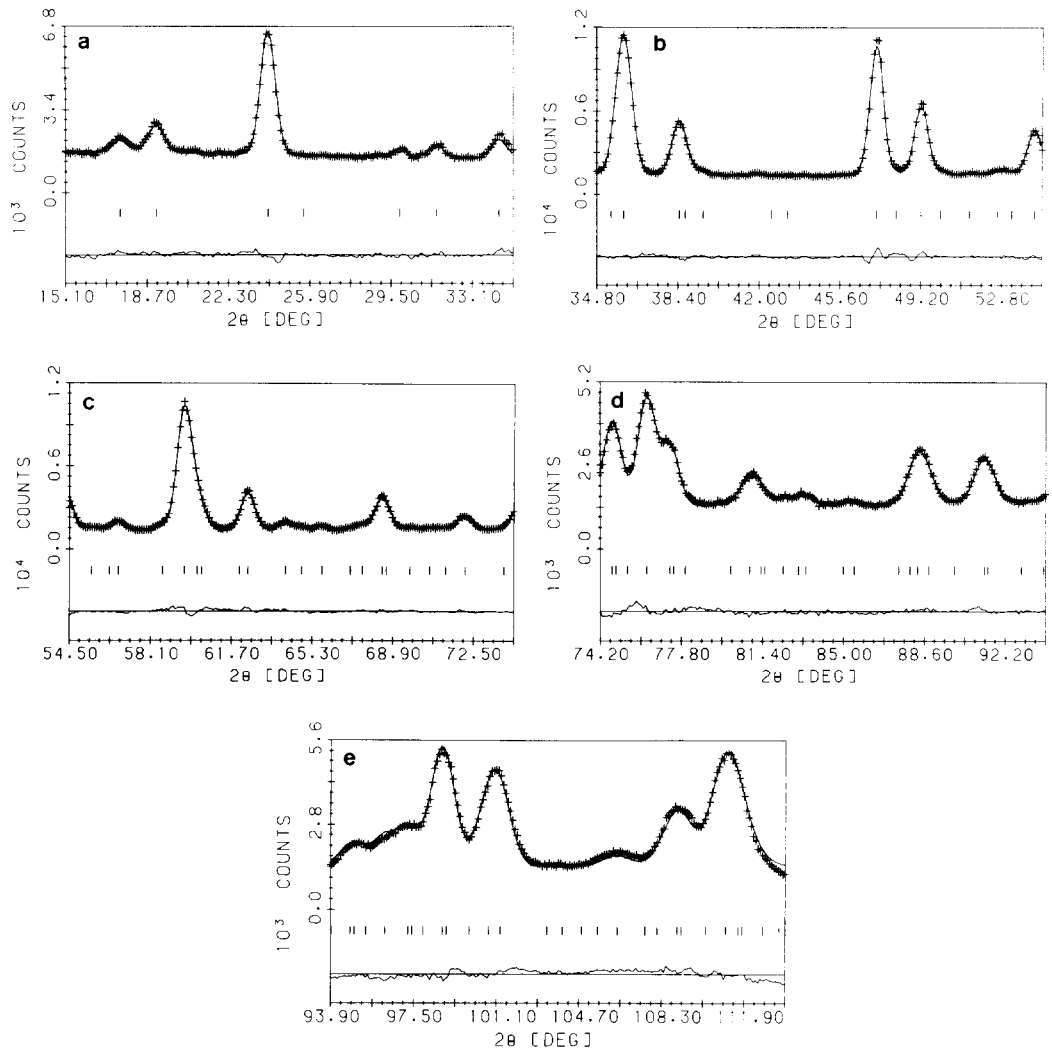

FIG. 2. The observed (+), calculated (−), and difference powder profiles for $CoTa_2O_6$ at 298 K (reflection positions are marked).

(Fig. 4), which has the same functional form as the magnetic portion of the heat capacity near T_c, according to Fisher (*13*). The λ anomaly at $T_c \approx 13.0$ K is obvious and indicates a phase transition. The slow decay of the heat capacity from 14 to 50 K shows clearly that a large amount of the entropy gain on warming the sample occurs above T_c. This is strong additional evidence that significant short-range ordering of a low-dimensional nature is taking place.

The data between 100 and 300 K were corrected for diamagnetism and fitted (Fig. 5) to a Curie–Weiss relationship,

$$\chi^{-1} = (T - \theta)/C,$$

giving $\mu_{eff} = 4.62(1)\ \mu_B$ and $\theta = -32.4(3)$ K. The effective moment is typical for high-spin Co^{2+} in roughly octahedral geometry.

Susceptibility data for $CoTa_2O_6$ have been published previously and are not reproduced here (*2*).

TABLE II

BOND DISTANCES AND ANGLES AT ROOM TEMPERATURE IN $CoSb_2O_6$

Bond	Distance (Å)		Expected (12)	Angle (°)	
Co–O	2.026(3)	Co–O_1	2.085[a]	180.00(0)	O_1–Co–O_1
	2.068(3)	Co–O_2		180.00(0)	O_2–Co–O_2
				102.3(2)	O_2–Co–O_2
				90.0(1)	O_1–Co–O_2
				77.7(2)	O_2–Co–O_2
Sb–O	1.987(6)	Sb–O_2		178.9(3)	O_1–Sb–O_2
	1.978(6)	Sb–O_1	1.96	175.0(6)	O_2–Sb–O_2
	1.992(2)	Sb–O_2		99.59(4)	O_1–Sb–O_2
				91.9(3)	O_1–Sb–O_2
				88.1(2)	O_2–Sb–O_2
				81.6(3)	O_2–Sb–O_2
				79.3(3)	O_1–Sb–O_1

[a] For Co^{2+} in a high-spin state.

TABLE IV

BOND DISTANCES AND ANGLES AT ROOM TEMPERATURE IN $CoTa_2O_6$

Bond	Distance (Å)		Expected (12)	Angle (°)	
Co–O	2.082(2)	Co–O_1	2.085[a]	180.00(0)	O_1–Co–O_1
	2.101(3)	Co–O_2		180.00(0)	O_2–Co–O_2
				99.2(1)	O_2–Co–O_2
				90.0(1)	O_1–Co–O_2
				80.7(1)	O_2–Co–O_2
Ta–O	1.974(4)	Ta–O_2		177.4(3)	O_2–Ta–O_2
	1.988(1)	Ta–O_2	2.08	175.6(2)	O_1–Ta–O_2
	2.006(3)	Ta–O_1		97.25(6)	O_1–Ta–O_2
				91.0(2)	O_1–Ta–O_2
				89.1(1)	O_2–Ta–O_2
				87.2(2)	O_2–Ta–O_2
				78.3(2)	O_1–Ta–O_1

[a] For Co^{2+} in a high-spin state.

Magnetic Structure of $CoSb_2O_6$

Below 13 K magnetic reflections appear at low angles in the diffraction pattern which are not indexable on the chemical unit cell. These super-lattice reflections can be indexed with a magnetic unit cell ($2a$, a, $2c$) or (a, $2a$, $2c$). The intensities were modeled by a profile refinement (Fig. 6) of the 7.5 K data set. The nuclear structure, cell constants, and peak width parameters were held fixed from the 20 K refinement. Two magnetic structures, which are indistinguishable from powder data, were found to be consistent with the reflection intensities. The structures (Fig. 7) can be described in terms of two sublattices (origin and the body center) where the moments within one sublattice are antiparallel along [100] and [001] but parallel along [010]. All moments lie within the ab plane along [110] and [1$\bar{1}$0]. The structures differ in the angle

TABLE III

CRYSTALLOGRAPHIC PARAMETERS FOR $CoTa_2O_6$ AT ROOM TEMPERATURE

Atom	Position	x	y	z	B(Å^2)
Co	$2a$	0	0	0	0.9(3)
Ta	$4e$	0	0	0.3304(4)	0.48(5)
O_1	$4f$	0.3109(7)	0.3109(7)	0	0.48(9)
O_2	$8j$	0.2967(4)	0.2967(4)	0.3255(4)	0.92(6)

R_{wp}	4.4%
R_p	3.4%
R_{nuc}	4.9%
R_{exp}	1.8%
No. of data points	995
Ind. reflections	97
d-Space range (Å)	0.833–4.58

Note. Space group $P4_2/mnm$; Z = 2; a = 4.7358(3) Å; c = 9.1708(7) Å; vol. = 205.68(3) Å^3.

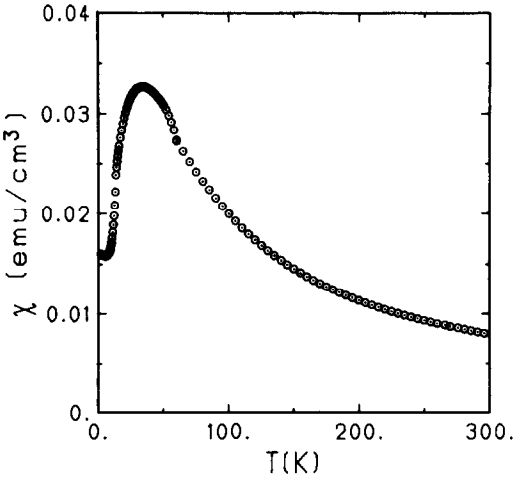

FIG. 3. Magnetic susceptibility data for $CoSb_2O_6$ measured at 100 G from 4 to 60 K and at 5000 G from 60 to 300 K.

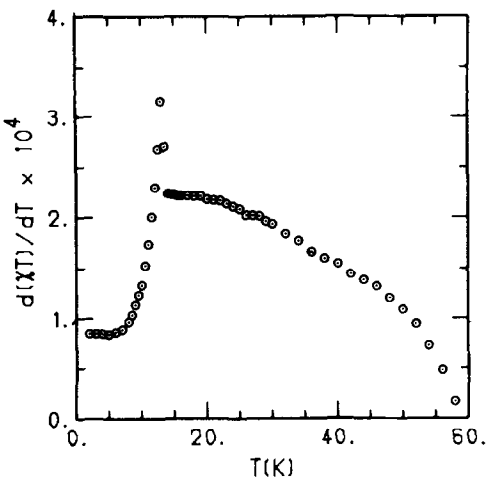

FIG. 4. Fisher's heat capacity obtained from the low-field susceptibility data for $CoSb_2O_6$ showing a λ anomaly at 13 K and large entropy gain above T_c.

of the moments between the two sublattices. For the structure shown in Fig. 7a, the two sublattices are collinear and in Fig. 7b they are orthogonal. It is worth mentioning that other more complicated models with the origin sublattice antiparallel along [100] and the body-centered sublattice antiparallel along [010] will also give the same scattering intensities for powder data.

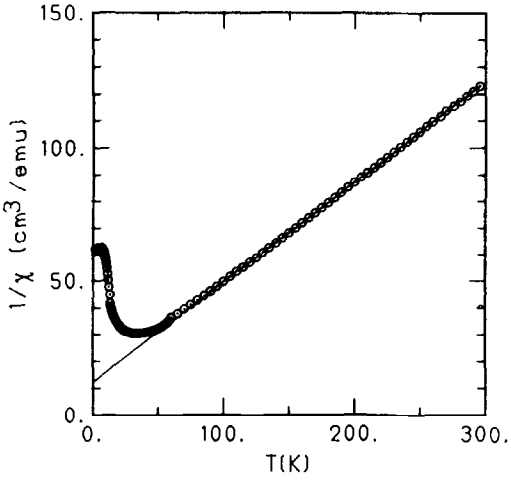

FIG. 5. Curie–Weiss law fit to the data shown in Fig. 3 giving $\mu_{eff} = 4.62(1)\ \mu_B$ and $\theta = -32.4(3)$ K.

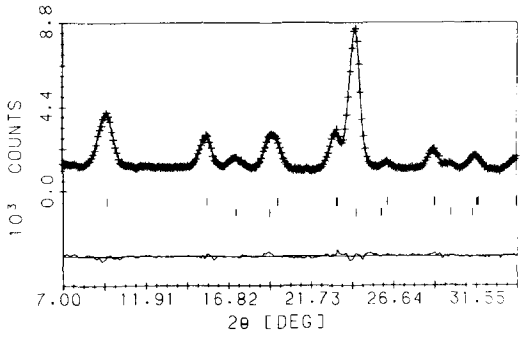

FIG. 6. Observed (+), calculated (−), and difference profiles of the neutron powder data for $CoSb_2O_6$ at 7.5 K. Bragg angles of nuclear reflections (bottom line) and magnetic reflections (top line) are indicated.

The same magnetic structure has also been observed in $FeTa_2O_6$ (*1*) where the two sublattices were determined to be orthogonal from Mössbauer data.

Magnetic Structure of $CoTa_2O_6$

The magnetic structure for this compound is significantly more complicated. The smallest supercell that indexes all of the well-defined magnetic reflections is a $2\sqrt{2}a \times 4c$ unit cell. In order to simplify the task of modeling the intensities, the structure was analyzed in terms of a helical spin arrangement (*14*). All magnetic reflections could be indexed with a helix propagation vector $\mathbf{k}_0 = (\frac{1}{4}, \frac{1}{4}, \frac{1}{4})$. The relative intensities

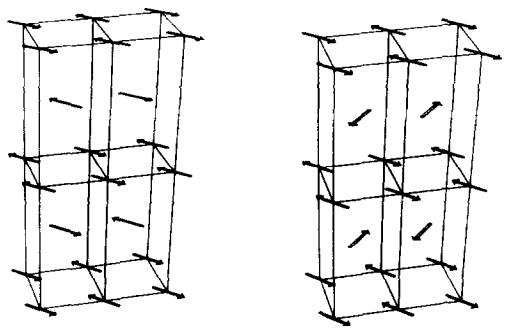

FIG. 7. Schematic illustrations of the $(2a, a, 2c)$ magnetic unit cell of $CoSb_2O_6$ at 7.5 K. The collinear model is shown on the left and the orthogonal model on the right.

for a helical spin structure are determined by the phase difference between the sublattices (corner and body center in this case) and the so-called "cone axis" about which the spins rotate (*8, 14, 15*). Attempts were made to model the magnetic reflections by refining the phase difference and the cone axis direction using the Rietveld method, without success. A somewhat more elaborate model in which the two sublattices have different cone axes was much more successful. The scattering cross section for this type of structure is derived in the Appendix and reproduced below:

$$\sigma(\mathbf{e}) = \tfrac{1}{4}\gamma r_0 S^2 f^2\{1 + [(\hat{\mathbf{e}}\cdot\mathbf{z}_1)^2 + (\hat{\mathbf{e}}\cdot\mathbf{z}_2)^2]/2 + \mathrm{Cos}(\pi[h+k+l])[\mathbf{x}_1\cdot\mathbf{x}_2 + \mathbf{y}_1\cdot\mathbf{y}_2 - (\hat{\mathbf{e}}\cdot\mathbf{x}_1)(\hat{\mathbf{e}}\cdot\mathbf{x}_2) - (\hat{\mathbf{e}}\cdot\mathbf{y}_1)\cdot(\hat{\mathbf{e}}\cdot\mathbf{y}_2)]\}\delta(\mathbf{K}\pm\mathbf{k}_0-\mathbf{e})$$

Here $\mathbf{z}_1$ and $\mathbf{z}_2$ are unit vectors along the cone axes of the two sublattices, $\hat{\mathbf{e}}$ is the unit neutron scattering vector, $\mathbf{K}$ is a reciprocal lattice vector, f is the magnetic form factor, and S is the magnetic moment in Bohr magnetons. $\mathbf{x}_v$ and $\mathbf{y}_v$ form an orthonormal basis with the corresponding $\mathbf{z}_v$, for both sublattices, and their orientation is related to the phase of the helix on sublattice v. Only the phase difference between the sublattices, and not the absolute phase, is important. Thus there are now five independent parameters that determine the relative intensities of the magnetic reflections as opposed to three for the one-cone axis model. The spin vector on sublattice v at lattice site n can be expressed as

$$\mathbf{S}(\mathbf{R}_{nv}) = [\mathbf{x}_v\cos(\mathbf{k}_0\mathbf{R}_{nv}) + \mathbf{y}_v\sin(\mathbf{k}_0\mathbf{R}_{nv})]S_v$$

and the basis vectors $\mathbf{x}_v$, $\mathbf{y}_v$ are related by Euler angles to the crystallographic basis via the following transformation matrix (*16*):

$$\begin{pmatrix}\hat{\mathbf{x}}\\ \hat{\mathbf{y}}\\ \hat{\mathbf{z}}\end{pmatrix} = \begin{pmatrix}\mathrm{Cos}\,\phi\,\mathrm{Cos}\,\beta\,\mathrm{Cos}\,\alpha - \mathrm{Sin}\,\phi\,\mathrm{Sin}\,\alpha & \mathrm{Cos}\,\phi\,\mathrm{Cos}\,\beta\,\mathrm{Sin}\,\alpha + \mathrm{Sin}\,\phi\,\mathrm{Cos}\,\alpha & -\mathrm{Cos}\,\phi\,\mathrm{Sin}\,\beta\\ -\mathrm{Sin}\,\phi\,\mathrm{Cos}\,\beta\,\mathrm{Cos}\,\alpha - \mathrm{Cos}\,\phi\,\mathrm{Cos}\,\alpha & -\mathrm{Sin}\,\phi\,\mathrm{Cos}\,\beta\,\mathrm{Sin}\,\alpha + \mathrm{Cos}\,\phi\,\mathrm{Cos}\,\alpha & \mathrm{Sin}\,\phi\,\mathrm{Sin}\,\beta\\ \mathrm{Sin}\,\beta\,\mathrm{Cos}\,\alpha & \mathrm{Sin}\,\beta\,\mathrm{Sin}\,\alpha & \mathrm{Cos}\,\beta\end{pmatrix}\begin{pmatrix}\hat{\mathbf{a}}\\ \hat{\mathbf{b}}\\ \hat{\mathbf{c}}\end{pmatrix}$$

A Rietveld refinement was carried out on the 4.2 K data set, with atomic positions fixed from the 10 K data set. Overall scale factor, linear background, zero angle, half-width parameters U, V, and W, cell constants, magnetic moment, and five Euler angles were refined. Two models with almost identical scattering intensities were found that gave a reasonable fit to the data. In both models all of the angles except α_1 refined to within three standard deviations of regular angles and were thus fixed as such for the final stages of the refinement. The profile fit is shown in Fig. 8 and resulting magnetic parameters are shown in Table V.

The magnetic moments in Table V are quite reasonable when compared with other values for Co^{2+} (in an octahedral environment) measured by neutron diffraction (*17–19*). Schematic drawings of Model 2 are

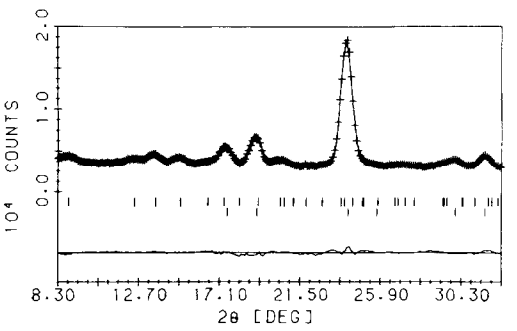

FIG. 8. Observed (+), calculated (−), and difference profiles of the neutron powder data for $CoTa_2O_6$ at 4.2 K. Bragg angles of nuclear reflections (bottom line) and magnetic reflections (top line) are indicated.

TABLE V

PARAMETERS FOR PROPOSED MAGNETIC STRUCTURES OF $CoTa_2O_6$ AT 4.2 K

	Model 1	Model 2
$\mathbf{k}_0$(rlu)	$(\frac{1}{4}, \frac{1}{4}, \frac{1}{4})$	$(\frac{1}{4}, \frac{1}{4}, \frac{1}{4})$
μ(BM)	3.25(2)	3.31(2)
α_1	45(2)	33(2)°
β_1	120°	0°
$\alpha_2-\alpha_1$	180°	90°
$\beta_2-\beta_1$	0°	135°
$\theta_2-\theta_1$	180°	0°
χ^2	5.9	5.8

shown in Fig. 9, indicating how the moments are oriented in the basal plane (Fig. 9a) and in the *ac* plane (Fig. 9b).

Critical Region for $CoSb_2O_6$

A log–log plot (Fig. 10) of magnetic moment versus reduced temperature ($t = (T_c - T)/T_c$) gives $\beta = 0.12(2)$ and $T_c = 12.64(5)$ K. Inspection of the 12.6 K profile refinement shows evidence of critical scattering about the magnetic peak at $2\theta = 9.65°$, which will cause the measured moment from the profile fit to be too large. The measured value of β is consistent only with

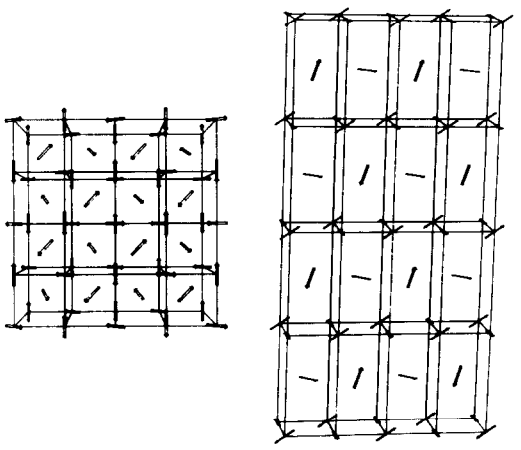

FIG. 9. Schematic illustrations of the *ab* face (left) and the *ac* face (right) of the (4*a*, 4*a*, 4*c*) magnetic unit cell for $CoTa_2O_6$.

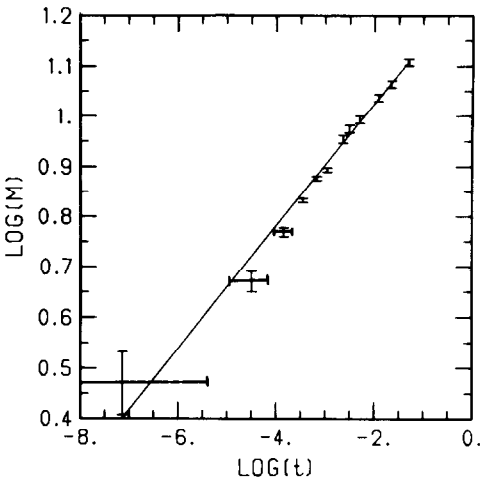

FIG. 10. Log–log plot of magnetic moment versus reduced temperature ($t = [T_c - T]/T_c$) giving $\beta = 0.12(2)$ and $T_c = 12.64(5)$ K.

2-D Ising behavior where β is known to be $\frac{1}{8}$. Usually β obtained from such data tends to be very correlated with the value chosen for T_c. However, in this case an increase in T_c of 0.1 K will yield $\beta = .13(2)$ (still in agreement with $\frac{1}{8}$), but χ^2 increases by a factor of 3 indicating that the β–T_c correlation is not very large.

The low-temperature magnetic reflections appear to be Bragg in nature and show no evidence that the ordered state is two dimensional. This indicates that a weak interplanar coupling is present which will only affect the critical properties close to T_c. We suspect that crossover to 3-D critical indices occurs above 12.64 K, which explains why the critical temperatures obtained from the heat capacity and susceptibility data are significantly higher. Similar crossover behavior has been observed previously with single-crystal neutron data in K_2NiF_4 (*20*) and Rb_2CoF_4 (*21*). No attempt was made to interpret the scattering between 12.64 and 13 K in terms of a 3-D Ising model due to the difficulty of correcting for the critical scattering which is already becoming important at 12.6 K.

TABLE VI

COMPARISON OF MAGNETIC AND STRUCTURAL PROPERTIES OF $CoSb_2O_6$ AND $CoTa_2O_6$

	$CoSb_2O_6$	$CoTa_2O_6$
T_{max}(K)	35(1)	15.6(2)
T_c(K)	13.0(2)	6.63(5)
Co–O_1 (Å)	2.026	2.082
O_1–O_1 (Å)	2.522	2.532
Magnetic cell	$a_M(b) = 2a$	$a_M(b) = 4a(2\sqrt{2}a)$
	$c_M = 2c$	$c_M = 4c$

Conclusions

In Table VI some selected magnetic and structural properties of $CoSb_2O_6$ and $CoTa_2O_6$ are compared. While the gross features of these isostructural materials are similar, both show dominant short-range order followed by a transition to long-range order at low temperatures, the quantitative differences are striking. For example T_c and $T(\chi_{max})$ are both greater by a factor of 2 for $CoSb_2O_6$ relative to $CoTa_2O_6$. Analysis of heat capacity data for $CoTa_2O_6$ is consistent with the anisotropic square planar Ising model with $J_1/J_2 \approx 60$ and $J_1 = 11.8$ K (*3*). Examination of Figs. 3 and 4 suggests a similar model for $CoSb_2O_6$. For the trirutile structure of composition MM'_2O_6, the dominant in plane exchange interaction involves a next-nearest-neighbor 180° *M*–O–O–*M* interaction along one diagonal of the square face as shown in Fig. 11. Other possible interactions between nearest neighbors involve at least one very long *M*–O distance and bond angles far from 180° or 90°. To a crude approximation this resembles a linear chain system, although, of course, the J_1/J_2 ratio is not large enough. Nonetheless, analysis in terms of a linear chain can be instructive. For example the temperature corresponding to the susceptibility maximum $T(\chi_{max})$ in the one-dimensional Ising model is a simple measure of J_1, the dominant exchange constant. Evidently, J_1 increases by about a factor of 2 in going from $CoTa_2O_6$ to $CoSb_2O_6$, as already noted. In the theory of superexchange, J_1 is proportional to the square of the transfer integral which is itself proportional to overlap integrals between metal ions and ligands which connect them to adjacent ions, (*22*). One would therefore expect J_1 to be highly sensitive to changes in relevant bond distances. From Table 6 the most significant change in going from $CoTa_2O_6$ to $CoSb_2O_6$ is a shortening of the Co–O_1 bond by about 3%. This bond is the one involved in the 180° Co–O–O–Co interaction. Note that no change occurs in the O_1–O_1 distance as expected. The observations are qualitatively consistent with the increase in $T(\chi_{max})$ for $CoSb_2O_6$.

Relating T_c to structural changes is much less straightforward as interplanar interactions may also be involved. Note also that the magnetic unit cell is smaller and the structure is simpler for $CoSb_2O_6$ than for $CoTa_2O_6$. In fact, it is the same as the one found previously in $FeTa_2O_6$ (*1*). This may

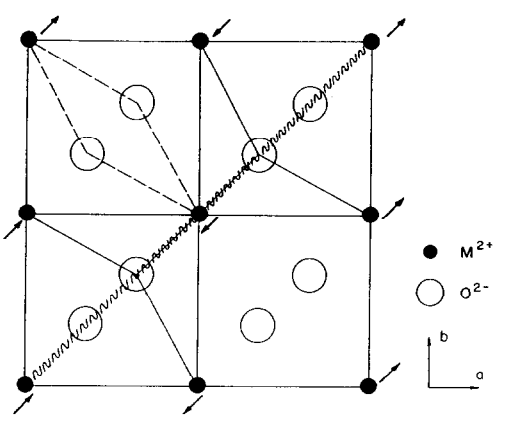

FIG. 11. Superexchange pathways in the *ab* plane for MTa_2O_6 trirutile. The arrows show the magnetic moments found in the 3-D ordered state for $CoSb_2O_6$.

indicate a greater degree of frustration in the tantalate relative to the antimonate, suggesting a larger J_1/J_2 for the later, but this has yet to be measured.

Acknowledgments

We thank Mr. G. Hewitson for considerable assistance in collecting the susceptibility data and M. F. Eitel for local software development and initial crystallographic work on $CoTa_2O_6$. Helpful discussions with M. F. Collins concerning the critical region are also greatly appreciated. We acknowledge financial assistance from the Natural Science and Engineering Research Council of Canada in the form of operating grants to J.E.G. and C.V.S., a postgraduate scholarship to J.N.R., and infrastructure support for the McMaster Nuclear Reactor.

Appendix

Helical spin structures can be represented by expanding the spin vectors in terms of Fourier components:

$$\mathbf{S}(\mathbf{R}_{nv}) = \Sigma_{\mathbf{k}}\mathbf{Q}_v(\mathbf{k}) \exp(i\mathbf{k} \cdot \mathbf{R}_{nv}), \quad (1)$$

where n labels a unit cell in the lattice and v labels the position of the spin within a unit cell. $\mathbf{k}$ is the propogation vector of the spiral; thus the repeat length of the spiral is $2\pi/k$. The Fourier components $\mathbf{Q}_v$ are complex and must satisfy the condition

$$\mathbf{Q}_v(\mathbf{k}) = \mathbf{Q}_v^*(-\mathbf{k}) \quad (2)$$

in order to insure reality of the spin vectors. For a one-$\mathbf{k}$ spiral with propagation vector $\mathbf{k}_0$ on sublattice v, in which the spins precess about an arbitrary axis, $\mathbf{z}_v$ (which is not necessarily collinear with $\mathbf{k}_0$), one can choose

$$\mathbf{Q}_v(\mathbf{k}_0) = \tfrac{1}{2}S_v(\mathbf{x}_v - i\mathbf{y}_v), \quad (3)$$

where S_v is the spin moment and $\mathbf{x}_v$, $\mathbf{y}_v$, and $\mathbf{z}_v$ form an orthonormal basis. Combining Eqs. (1), (2), and (3)

$$\mathbf{S}(\mathbf{R}_{nv}) = S_v[\mathbf{x}_v \cos(\mathbf{k}_0 \cdot \mathbf{R}_{nv}) + \mathbf{y}_v \sin(\mathbf{k}_0 \cdot \mathbf{R}_{nv})]. \quad (4)$$

The scattering cross section for such a structure can be calculated starting with the general expression for neutron magnetic scattering:

$$\sigma(\mathbf{e}) = \tfrac{1}{2}\gamma r_0\{|\mathbf{P}(\mathbf{e})|^2 - |\hat{\mathbf{e}} \cdot \mathbf{P}(\mathbf{e})|^2\} = \tfrac{1}{2}\gamma r_0|\mathbf{P}_\perp(\mathbf{e})|^2 \quad (5)$$

$$\mathbf{P}_\perp(\mathbf{e}) = \Sigma_{nv}f_v(e)\mathbf{S}_\perp(\mathbf{R}_{nv}) \exp(i\mathbf{e} \cdot \mathbf{R}_{nv}), \quad (6)$$

where $\mathbf{e}$ is the neutron scattering vector, f_v is the magnetic form factor, and $\mathbf{S}_\perp$ is the component of $\mathbf{S}$ in the scattering plane

$$\mathbf{S}_\perp = \mathbf{S} - \hat{\mathbf{e}}(\mathbf{S} \cdot \hat{\mathbf{e}}). \quad (7)$$

The factor $\frac{1}{2}\gamma r_0$ is the neutron scattering length per Bohr magneton and is equal to 0.27×10^{-12} cm. Combining (1), (6), and (7) one obtains

$$\begin{aligned}\mathbf{P}_\perp(\mathbf{e}) &= \Sigma_{\mathbf{k}}\Sigma_{nv}f_v(e)\mathbf{Q}_{\perp v}(\mathbf{k}) \exp[i(\mathbf{e} + \mathbf{k}) \cdot \mathbf{R}_{nv}] \\ &= \Sigma_{\mathbf{k}}\Sigma_{nv}f_v(e)\mathbf{Q}_{\perp v}(\mathbf{k}) \exp[i(\mathbf{e} + \mathbf{k}) \cdot (\mathbf{R}_n + \mathbf{r}_v)] \\ &= \Sigma_{\mathbf{k}}\Sigma_v f_v(e)\mathbf{Q}_{\perp v}(\mathbf{k}) \exp[i(\mathbf{e} + \mathbf{k}) \cdot \mathbf{r}_v] \times \Sigma_n \exp[i(\mathbf{e} + \mathbf{k}) \cdot \mathbf{R}_n] \\ &= \Sigma_{\mathbf{k}}\Sigma_v f_v(e)\mathbf{Q}_{\perp v}(\mathbf{k}) \exp[i(\mathbf{e} + \mathbf{k}) \cdot \mathbf{r}_v] \times \delta(\mathbf{e} + \mathbf{k} - \mathbf{K}), \quad (8)\end{aligned}$$

where $\mathbf{Q}_\perp$ is defined in the same way as $\mathbf{S}_\perp$ and $\mathbf{K}$ is a reciprocal lattice vector. For $CoTa_2O_6$ there are two sublattices $\mathbf{r}_1 = (0, 0, 0)$ and $\mathbf{r}_2, = (\frac{1}{2}, \frac{1}{2}, \frac{1}{2})$ with the same moment and form factor, i.e., $S_v = S$ and $f_v(e) = f(e)$ for $v = 1$ and 2.

$$\begin{aligned}|\mathbf{P}_\perp(\mathbf{e})|^2 &= f^2(e)\Sigma_{\mathbf{k}\mathbf{k}'}\delta(\mathbf{e} + \mathbf{k} - \mathbf{K})\delta(\mathbf{e} + \mathbf{k}' - \mathbf{K}') \\ &\times \Sigma_{vv'}\mathbf{Q}_{\perp v}(\mathbf{k}) \cdot \mathbf{Q}^*_{\perp v'}(\mathbf{k}') \exp[i(\mathbf{e} + \mathbf{k}) \cdot \mathbf{r}_v] \exp[-i(\mathbf{e} + \mathbf{k}') \cdot \mathbf{r}_{v'}]. \quad (9)\end{aligned}$$

For $\mathbf{k}$ not at the zone edge the two δ functions will only be nonzero if $\mathbf{k} = \mathbf{k}'$ and $\mathbf{e} = \mathbf{K} - \mathbf{k}$:

$$|\mathbf{P}_\perp(\mathbf{K} \mp \mathbf{k}_0)|^2 = f^2(e)\Sigma_{vv'}\mathbf{Q}_{\perp v}(\pm\mathbf{k}_0) \cdot \mathbf{Q}^*_{\perp v'}(\pm\mathbf{k}_0) \exp[i\mathbf{K} \cdot (\mathbf{r}_v - \mathbf{r}_{v'})], \quad (10)$$

where $\mathbf{k}_0$ is the helix propagation vector for which the Fourier components are non-

zero. Performing the double sum over the two sublattices one obtains

$$|\mathbf{P}_\perp(\mathbf{K} \mp \mathbf{k}_0)|^2 = f^2(e)\{|\mathbf{Q}_{\perp 1}|^2 + |\mathbf{Q}_{\perp 2}|^2 + 2Re[\mathbf{Q}_{\perp 1} \cdot \mathbf{Q}^*_{\perp 2} \exp[-i\mathbf{K} \cdot (\tfrac{1}{2}, \tfrac{1}{2}, \tfrac{1}{2})]]\} = f^2(e)\{|\mathbf{Q}_{\perp 1}|^2 + |\mathbf{Q}_{\perp 2}|^2 + 2\mathrm{Cos}[\pi(h + k + l)]Re(\mathbf{Q}_{\perp 1} \cdot \mathbf{Q}^*_{\perp 2})\}. \quad (11)$$

From 3 and 7

$$|\mathbf{Q}_{\perp v}|^2 = \tfrac{1}{4}S^2[1 + (\hat{\mathbf{e}} \cdot \mathbf{z}_v)^2] \quad (12)$$

and

$$\mathbf{Q}_{\perp 1} \cdot \mathbf{Q}^*_{\perp 2} = \tfrac{1}{4}S^2[(\mathbf{x}_1 - i\mathbf{y}_1) \cdot (\mathbf{x}_2 + i\mathbf{y}_2) - (\hat{\mathbf{e}} \cdot \mathbf{x}_1 - i\hat{\mathbf{e}} \cdot \mathbf{y}_1)(\hat{\mathbf{e}} \cdot \mathbf{x}_2 + i\hat{\mathbf{e}} \cdot \mathbf{y}_2)]. \quad (13)$$

Finally

$$\sigma(\mathbf{e}) = \tfrac{1}{4}\gamma r_0 S^2 f^2\{1 + [(\hat{\mathbf{e}} \cdot \mathbf{z}_1)^2 + (\hat{\mathbf{e}} \cdot \mathbf{z}_2)^2]/2 + \mathrm{Cos}(\pi[h + k + l])(\mathbf{x}_1 \cdot \mathbf{x}_2 + \mathbf{y}_1 \cdot \mathbf{y}_2 - \hat{\mathbf{e}} \cdot \mathbf{x}_1\hat{\mathbf{e}} \cdot \mathbf{x}_2 - \hat{\mathbf{e}} \cdot \mathbf{y}_1\hat{\mathbf{e}} \cdot \mathbf{y}_2)\}\delta(\mathbf{K} \pm \mathbf{k}_0 - \mathbf{e})$$
$$= \tfrac{1}{4}\gamma r_0 S^2 f^2\{1 + [(\hat{\mathbf{e}} \cdot \mathbf{z}_1)^2 + (\hat{\mathbf{e}} \cdot \mathbf{z}_2)^2]/2 + \mathrm{Cos}(\pi[h + k + l])[\mathbf{x}_{\perp 1} \cdot \mathbf{x}_{\perp 2} + \mathbf{y}_{\perp 1} \cdot \mathbf{y}_{\perp 2}]\}\delta(\mathbf{K} \pm \mathbf{k}_0 - \mathbf{e}).$$

The cross section for a one-cone axis structure presented by Corlis and Hastings (*15*) is retrieved by setting $\mathbf{x}_1 = \mathbf{x}_2$, $\mathbf{y}_1 = \mathbf{y}_2$ and $\mathbf{z}_1 = \mathbf{z}_2$.

References

1. S. M. Eicher, J. E. Greedan, and K. J. Lushington, *J. Solid State Chem.* **62,** 220 (1986).
2. R. K. Kremer and J. E. Greedan, *J. Solid State Chem.* **73,** 579 (1988).
3. R. K. Kremer, J. E. Greedan, E. Gmelin, W. Dai, and M. A. White, Proceedings of International Conference on Magnetism, Paris, 1988, *J. de Phys.* **49,** C8–1495 (1988).
4. H. Kasper, *Mh. Chem.* **98,** 2107 (1967).
5. Bayer, *Ber. Dtsch. Keram. Ges.* **39,** 11, 535–504 (1962).
6. S. M. Eicher, Ph.D. dissertation, McMaster University (1984).
7. J. N. Reimers, J. E. Greedan, and M. Sato, *J. Solid State Chem.* **72,** 390 (1988).
8. J. N. Reimers, J. E. Greedan, *J. Solid State Chem.*
9. H. M. Rietveld, *J. Appl. Crystallogr.* **2,** 65 (1969).
10. L. Koester, *Springer Tracts Mod. Phys.* **80,** 34 (1978).
11. R. E. Watson and A. J. Freeman, *Acta Crystallogr.* **14,** 27 (1961).
12. Shannon, R. D., *Acta Crystallogr. A* **32,** 751 (1976).
13. M. E. Fisher, *Philos. Mag.* **17,** 1731 (1962).
14. D. H. Lyons, T. A. Kaplan, K. Dwight, and N. Menyuk, *Phys. Rev.* **126,** 540 (1961).
15. J. M. Hastings and L. M. Corliss, *Phys. Rev.* **126,** 556 (1961).
16. G. Arfkin, "Mathematical Methods for Physicists," p. 198, Academic Press, New York (1985).
17. E. F. Bertaut, J. Coing-Boyat, and A. Delapalme, *Phys. Lett.* **3,** 178 (1963).
18. P. J. Brown and B. C. Frazer, *Phys. Rev.* **129,** 1145 (1962).
19. S. Nomura, R. Santoro, J. Fang, and R. Newnham, *J. Phys. Chem. Solids* **25,** 901 (1964).
20. R. J. Birgeneau, H. J. Guggenheim, and G. Shirane, *Phys. Rev. B* **1,** 2211 (1970).
21. E. J. Sammuelsen, *Phys. Rev. Lett.* **31,** 936 (1973).
22. P. W. Anderson, *Phys. Rev.* **115,** 2 (1959).